

The Virtual Synchronous Generator control for transient stability support in power systems with large-scale renewable plants

Daniel Carletti ^[1], Jussara Farias Fardin ^[2], Lucas Frizera Encarnação ^[3]

[1] danielc.ufes@gmail.com. [2] jussara.fardin@ufes.br. [3] lucas.encarnacao@ufes.br. Universidade Federal do Espírito Santo, Departamento de Engenharia Elétrica.

ABSTRACT

The dynamic security assessment of power systems is a critical activity to ensure a safe energy delivery to consumers and the study of transient stability is a fundamental part of this process. The power systems are experiencing a growth of large-scale renewable energy plants connected to the system, which in turn are connected to the grid by power converters that are not capable of contributing to the system inertial stabilization and, therefore, could compromise its transient stability. One way to mitigate this problem is to make these plants contribute to the system stabilization by adopting specific control strategies, such as the virtual synchronous generator (VSG), for their interface power converters. In this paper, a quantitative evaluation of the transient stability support of a VSG is proposed in large-scale applications. For this purpose, the stability assessment of a single-machine infinite-bus (SMIB) system with the VSG is done using transient stability metrics such as the critical clearing time (CCT) and the transient stability index (TSI). In addition, the same analysis is made for a conventional synchronous machine (SM) and the results are compared and discussed. Furthermore, the VSG parameters adaptability is presented as an alternative to optimizing the system stability.

Keywords: Transient stability. Critical clearing time. Power systems. Virtual Synchronous generator.

RESUMO

A avaliação da estabilidade de sistemas elétricos é uma atividade fundamental para garantir uma entrega de energia segura para os consumidores, tendo o estudo da estabilidade transiente do sistema como uma etapa fundamental. Os sistemas elétricos experimentam uma expansão na geração de energia renovável em plantas de grande porte que, por sua vez, são conectadas a rede por meio de conversores de potência. No entanto, esses conversores não possuem a capacidade natural de contribuir para a estabilização inercial do sistema e podem comprometer sua estabilidade. Uma forma de mitigar tal problema é fazer com que esses conversores contribuam para a estabilidade adotando estratégias de controle como o gerador síncrono virtual (VSG). Neste artigo, uma avaliação quantitativa da contribuição para a estabilidade transiente do VSG é proposta. Para isso, a análise da estabilidade transiente de um sistema gerador-barras infinita (SMIB) com o VSG é realizada utilizando métricas de estabilidade como o tempo crítico de falta (CCT) e o índice de estabilidade transiente (TSI). Além disso, a mesma análise é realizada para uma máquina síncrona e os resultados em ambos os casos são comparados e discutidos. Por fim, a adaptabilidade dos parâmetros do VSG é apresentada para otimizar a estabilidade do sistema.

Palavras-chave: Estabilidade transiente. Tempo crítico de falta. Sistemas elétricos de potência. Gerador síncrono virtual.

Nomenclature			
AC	Alternate Current	PEBS	Potential Energy Boundary Surface
AVR	Automatic Voltage Regulator	PSAT	Power System Analysis Toolbox
CCT	Critical Clearing Time	PV	Photovoltaic Source
DAE	Differential and Algebraic Equations	RES	Renewable Energy Sources
DC	Direct Current	SEP	Stable Equilibrium Point
DG	Distributed Generator	SM	Synchronous Machine
EAC	Equal Area Criterion	SMIB	Single Machine Infinite Bus
EEAC	Extended Equal Area Criterion	TEF	Transient Energy Function
LS-PV	Large Scale Photovoltaic	TSI	Transient Stability Index
LS-PWM	Level-Shifted Pulse-Width Modulation	UEP	Unstable Equilibrium Point
NPC	Neutral Point Clamped	VSI	Voltage Source Inverter
PCC	Point of Common Coupling	VSG	Virtual Synchronous Machine
PD	Phase Disposition	WTG	Wind Turbine Generator

1 Introduction

As the power systems evolved in size and complexity new forms of instability emerged bringing up the need for a constant update for the engineers that work in the system planning and operation. Nowadays, the power system stability follows a standard classification based on the system variable affected by the instability (frequency, voltage, and rotor angle), the size of the disturbance considered and the time span to determine the instability of the system. The rotor angle stability for large disturbances, also known as transient stability, is concerned with the ability of the system to maintain its generating units in synchronism after being subjected to a severe disturbance such as a fault or a critical line contingency. The time frame in which transient stability occurs is generally of a few seconds following the disturbance (KUNDUR, 1994; KUNDUR *et al.*, 2004). As a result, studying ways to prevent or mend the problems that appear with this type of instability must be accounted for before the system becomes operational.

Moreover, the growth of renewable energy sources (RES) connected to the system, many of them with static power converters as an interface brings up some of these instability problems that render the utilization and development of these energy sources a challenge to be dealt with. These RES, mainly solar photovoltaic (PV) and wind-turbine-generator (WTG) systems are commonly added to the grid in two possible forms: dispersed in the low voltage distribution system through small-scale distributed generators (DG), or in large-scale generating units (LS-RES) connected to the main transmission and sub-transmission system.

Due to the exponential growth in the use of WTG for power generation over the last decade, many

were the efforts to evaluate the impacts that different WTG sizes and technologies have on the system stability, especially transient stability (GAUTAM; VITTAL; HARBOUR, 2009; CHOWDHURY *et al.*, 2013; SHI *et al.*, 2014). However, stability in the presence of non-rotational LS-RES, like PV, still is a topic in development. Some of the LS-PV (large-scale photovoltaic) projects that are in development or operational are: Topaz solar farm (550 MW) and Desert Sunlight Solar Farm (550 MW) in California, Yanchi Solar PV Station (1000 MW) in China, among other existing projects (PVRESOURCES, 2020).

This type of power plant does not have any native rotational inertia and as a result, it does not participate directly in the voltage and frequency stabilization of AC systems. The system interface is done by power converters aiming to inject the maximum generated power instantaneously. Therefore, the system is subjected to the solar irradiation and temperature intermittency that add uncertainty in the system operation, which could lead to voltage and frequency fluctuations. In Shah *et al.* (2015) and Ding *et al.* (2016), the challenges that need to be addressed for a stable and secure implementation of LS-PV in the system are highlighted. The transient instability is cited as one of the main concerns for the future of LS-PV. In Cabrera-Tobar *et al.* (2016), national grid-codes from various countries are presented and is noted that some countries are already following requirements for Fault-Ride-Through in LS-PV. Additionally, some efforts have been made towards studying the impacts of LS-PV. In Tan and Kirschen (2007), Eftekharijad *et al.* (2013), Bueno, Hernández and Ruiz-Rodriguez (2016), the authors show that LS-PV added to the grid could have both benefits and downsides depending on a number of variables such as disturbance type,

the control strategy used by the interface converters, fault location, PV penetration levels and the system topology in the study.

In the meantime, the last decade saw a new approach for the control strategy applied to these non-rotational RES interface converters. The idea was to make these converters mimic a synchronous machine (SM) dynamic behavior by embedding a proper machine model in the control scheme. Thus, the converter could aid in the system stabilization due to its virtual inertia characteristic (BECK; HESSE, 2007; DRIESEN; VISSCHER, 2008). This proposal received different names in the literature (ENCARNAÇÃO et al., 2018), however, in this paper we'll be referring to it as a virtual synchronous generator (VSG).

Moreover, despite the VSG-based control using a SM model in its implementation, it is not restricted by real machines' constructive parameters. Parameters such as the reactance, armature resistance, and notably the machine's inertia constant are not fixed and could be adjusted for better system response. These could even be tuned in real-time during operation when the VSG is being subjected to disturbances in the system. Some papers suggest an adaptive control for just the inertia constant when others state that a coordinated control between both inertia constant and damping coefficient is most suitable (TORRES et al., 2014; ALIPOOR; MIURA; ISE, 2015; LI et al., 2017). However, the use of adaptive controls for the VSG parameters on the literature always focused in the frequency stability of small-scale DGs. Also, the VSG stability assessment for large-disturbance scenarios is not common in the literature and only found with qualitative analysis of voltage, frequency, and power curves with time without using specific metrics for transient stability analysis.

In this paper, a novel quantitative approach to large-scale VSG support for transient stability in power systems is proposed by employing two metrics used in power system transient stability assessment, the critical clearing time (CCT), and the transient stability index (TSI). Using such metrics in a single-machine infinite-bus (SMIB) system, the paper performs a quantitative analysis between the dynamic behavior of a VSG added to the system and a conventional SM undergoing different fault scenarios. The VSG parameters adaptability is also evaluated by means of the stability metrics chosen and proved to be a promising alternative for future large-scale applications. This novel approach to visualize the VSG impact on transient stability in power systems opens the possibility for a new form of adaptive control for VSG

parameters in which the metrics (CCT and TSI) could be used as objective functions to optimize stability.

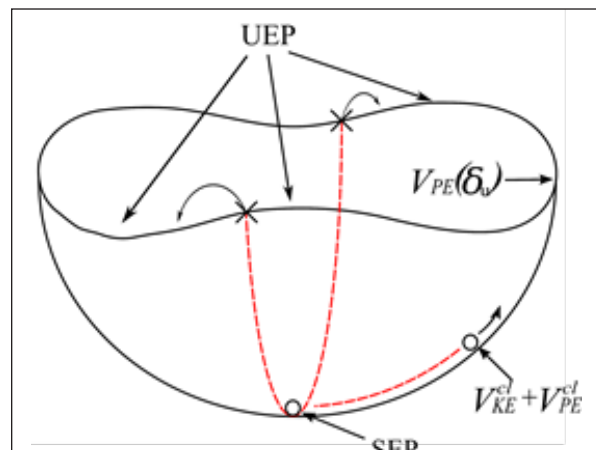
The structure of this paper is as follows. Section 2 presents a theoretical approach to the problem. Section 3 presents the proposed VSG-based control topology. Section 4 presents a discussion about the results obtained and, finally, Section 5 presents the conclusions.

2 Transient Stability analysis

The power system can be mathematically represented by a set of differential and algebraic equations (DAE) that model the behavior of the different devices connected to it and the power flow. A common way to study the stability of a system is by analytically solving this DAE set through numerical integration using a time-domain approach. However, for large power systems with multiple generators, this approach can be complex and demand a high computational effort. On the other hand, direct methods of stability analysis handle the problem without explicitly solving the differential equations of the system. The foundation for the method is Lyapunov's second method, in which the transient energy function is commonly adopted as a valid Lyapunov function. This method is also known as the transient energy function (TEF) method and was, in the last few decades, widely used for transient stability analysis of multimachine systems (KUNDUR, 1994; SAUER; PAI; CHOW, 2017). For a better understanding of the method's principle, Figure 1 is shown.

Figure 1 illustrates a ball rolling on the inner surface of a bowl. The ball is subjected to a kinetic energy injection, and because of that, it develops an exit movement from its initial stable equilibrium point (SEP).

Figure 1 – Visual description of the direct method for stability analysis.



Source: authors.

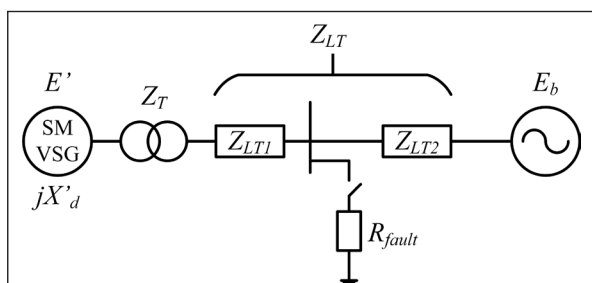
If the ball is not capable of converting all its excess kinetic energy before reaching the rim of the bowl, it will no longer return to a SEP inside the bowl and the system is deemed unstable. On the contrary, the ball will return to a new SEP and the system is considered stable. The analogy with power systems transient stability is made by considering the ball as one generator that gains kinetic (V_{KE}^{cl}) and potential (V_{PE}^{cl}) energy by the acceleration imposed during a fault in the system.

The rim of the bowl is related to the potential energy boundary surface (PEBS) and is created by a set of unstable equilibrium points (UEP) of the system defined by the potential energy in each one. After the fault clearance, the post-fault system must be capable of absorbing the excess kinetic energy so that the system can operate in a new SEP. In this paper, the TEF method for a SMIB system is shown in the next sections with the introduction of the TSI and CCT as transient stability metrics.

2.1 The energy function for SMIB systems

The classical representation of a SMIB system is shown in Figure 2, where E' is the generator internal voltage, Z_T is the generator transient reactance, Z_{LT} is the transformer impedance, Z_{LT1} is the total impedance of the transmission line, Z_{LT2} is the fault resistance to ground and E_b is the infinite bus voltage. The motion equations in p.u. for the synchronous generator are defined in Equations 1 and 2. The electrical power output of the machine (P_e) is defined by Equation 3.

Figure 2 – SMIB test system.



Source: authors.

$$\frac{2H}{\omega_0} \frac{d\omega}{dt} = P_m - P_e \quad (1)$$

$$\frac{d\delta}{dt} = \omega \quad (2)$$

$$P_e = C \sin \delta - D \cos \delta \quad (3)$$

In Equations 1-3, H is the inertia constant, ω is the rotor speed, ω_0 is the system synchronous speed, δ is the rotor angle, P_m is the mechanical input power, and C and D are variables depending on the induced voltage, resistances and reactance of the machine.

Associating Equations 1 and 2 and substituting Equation 3 on the resulting equation gives the second-order swing equation for the SM as shown in Equation 4.

$$\frac{2H}{\omega_0} \frac{d^2\delta}{dt^2} = P_m - C \sin \delta - D \cos \delta \quad (4)$$

The transient energy equation is obtained from manipulating Equation 4 and is shown in Equation 5. Details of the derivation of TEF for SMIB and multimachine systems can be found in (FOUAD; VITTAL, 1988; SAUER; PAI; CHOW, 2017). The TEF can be split into different energy terms that can be interpreted as follows:

- $\frac{2H\omega_0\omega^2}{2}$ – change in rotor kinetic energy;
- $P_m(\delta - \delta_s)$ – change in rotor position energy;
- $C(\cos \delta - \cos \delta_s)$ – change in magnetic stored energy;
- $\int_{\delta_s}^{\delta} D \cos \delta d\delta$ – change in dissipated energy.

Neglecting the system transfer conductances the TEF assumes the form in Equation 6, where P_m is the maximum post-fault power between the infinite bus and the generator. It must be noted that the TEF is always defined for the post-disturbance system.

The reference angle δ_s in Equation 6 refers to the SEP, and for the SMIB system, it can be calculated by Equation 7, where P_e^{max} is the maximum pre-fault power between the infinite bus and the generator.

$$V(\omega, \delta) = \frac{2H\omega_0\omega^2}{2} - P_m(\delta - \delta_s) - C(\cos \delta - \cos \delta_s) + \int_{\delta_s}^{\delta} D \cos \delta d\delta \quad (5)$$

$$V(\omega, \delta) = \frac{2H\omega_0\omega^2}{2} - P_m(\delta - \delta_s) - P_{e_{fault}}^{max}(\cos \delta - \cos \delta_s) \quad (6)$$

$$\delta_s = \sin^{-1}\left(\frac{P_m}{P_{e_{pre-fault}^{max}}}\right) \quad (7)$$

The Equation 8 shows the calculation for a SMIB system, where E_g is the generator internal voltage, E_b is the infinite bus voltage and X_T is the sum of all reactances between the two buses (imaginary parts of Z_{LT1} , Z_{LT2} , Z_T , and the generator transient reactance).

$$P_{e_{pre-fault}^{max}} = \frac{E' E_b}{X_T} \quad (8)$$

The closest UEP provides a good assessment of the system stability, in which the potential energy reaches its maximum value while being zero for the SEP. In the fault clearance moment, however, the transient energy is composed of kinetic and potential parts, as described by

$$V^{cl}(\omega_{cl}, \delta_{cl}) = V_{KE}^{cl} + V_{PE}^{cl} \quad (9)$$

where V_{KE}^{cl} is the kinetic energy given by the first term of Equation 6 and V_{PE}^{cl} is the potential energy given by the sum of the potential energy terms in the same equation. Both energy parts are calculated in the fault clearing moment defined by the rotor speed and angle, ω_{cl} , and δ_{cl} . The system is considered stable if the energy calculated for the UEP conditions is greater than the energy calculated for the fault clearing moment. Equation 10 defines the region of stability for the direct method based on the TEF.

$$V^{cl}(\omega_{cl}, \delta_{cl}) = V_{KE}^{cl} + V_{PE}^{cl} < V_{PE}(\delta_u) \quad (10)$$

2.2 Transient stability index (TSI) calculation

Using the transient stability definition presented in the last section, a metric for stability assessment is formulated. The TSI (Transient Stability Index) indicates if the system is stable or unstable and the system able to absorb kinetic energy beyond needed, in other words, it also indicates the level of stability in the system. The TSI is calculated by Equation 11 (CHOWDHURY et al., 2013).

$$TSI = \frac{V_{PE}(\delta_u) - V^{cl}(\omega_{cl}, \delta_{cl})}{V_{PE}(\delta_u)} \times 100\% \quad (11)$$

$V_{PE}(\delta_u)$ is the potential energy for the UEP and is calculated by the sum of potential energy terms in Equation 6 for a rotor angle relative to the UEP, which is calculated by Equation 12 for a SMIB system.

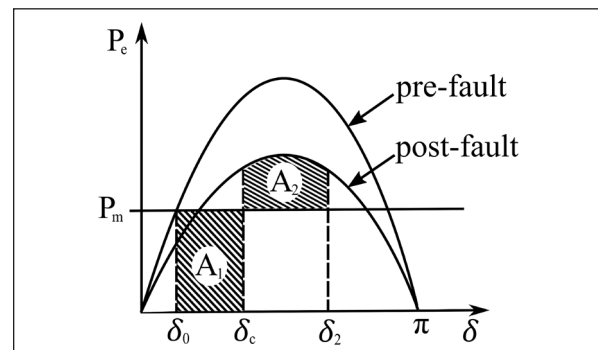
$$\delta_u = \pi - \delta_s \quad (12)$$

If the TSI is a positive value the system is deemed stable, otherwise it is considered unstable. The index value indicates the system's ability to further absorb energy in a stable case or the extra energy that needed to be absorbed for the system to become stable in an unstable scenario.

2.3 Equal area criterion and the critical clearing time (CCT)

The Equal Area Criterion (EAC) (GRAINGER; STEVENSON, 1994) is a graphical-analytical method used for transient stability assessment for SMIB systems, two interconnected machine systems and also multimachine systems by aggregating the multiple machines into a two equivalent machine system, the case for which the method was called Extended Equal-Area Criterion (EEAC) (XUE; VAN CUSTEM; RIBBENS-PAVELLA, 1989). The method is based on the analysis of the power-angle curves for the pre-fault and post-fault systems shown in Figure 3.

Figure 3 – Equal-area criterion.



Source: authors.

The areas A_1 and A_2 are calculated by the integral of the power-angle curve of the system given appropriate superior and inferior limits. The equivalence between EAC and TEF methods can be easily proved and is detailed in (KUNDUR, 1994; SAUER; PAI; CHOW, 2017). Area A_1 represents the kinetic energy injected in the system during the fault

occurrence while A_2 is related to the system capability of absorbing this excess energy. This equivalence is defined in Equations 13 and 14. The critical angle defining the transient stability limit is calculated by making A_1 equal to A_2 and manipulating the equation properly, the result is shown in Equation 15 .

$$A_1 = V_{KE}^{cl} = \frac{2H\omega_0\omega^2}{2} \quad (13)$$

$$A_2 = V_{PE}(\delta_u) - V_{PE}(\delta_{cl}) \quad (14)$$

$$\delta_{cr} = \cos^{-1}[(\pi - 2\delta_0) \sin \delta_0 - \cos \delta_0] \quad (15)$$

The maximum time the system can stay faulted before the machine rotor angle accelerates to the critical value is calculated as in Equation 16. To find this Critical Clearing Time (CCT) the critical angle found in Equation 15 is used as a parameter in the integration of the swing equation in Equation 4.

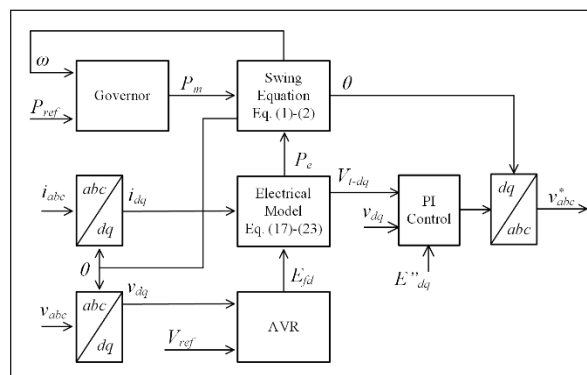
$$t_{cr} = \sqrt{\frac{4H(\delta_{cr} - \delta_0)}{\omega_s P_m}} \quad (16)$$

The CCT is usually considered an excellent indicator of the system transient stability and to rank different types of contingency. The EAC and the TEF method presented in this section are only valid for first swing stability. For post first swing stability, a small-signal analysis must be performed.

3 VSG-based control

The concept of a VSG-based control is to provide the power converter operation an inertial behavior. Hence, the implementation principle of a VSG-based control is based directly on the application in the converter control of the mechanical swing equations of a SM, Equations 1 and 2. In addition to the swing equations, voltage output and active power/frequency regulators are needed to properly synchronize the converter with the grid. A classic VSG implementation is illustrated in Figure 4.

Figure 4 – Typical VSG implementation topology including AVR and Governor.



Source: adapted from Encarnação et al. (2018).

The voltage and frequency regulators are identified respectively as Automatic Voltage Regulator (AVR) and Governor. A number of VSG control algorithms have been developed each with different characteristics such as machine model order applied, additional voltage, and frequency controls adopted and output reference of the control. An extended review of VSG-based controls can be found in Encarnação et al. (2018).

For the purposes of this paper, the implemented VSG will follow the topology presented in Figure 4. In the diagram shown in Figure 4, i_{abc} and v_{abc} are measured in the point of common coupling (PCC) with the grid. The output reference PI (Proportional Integral) control adjusts the terminal voltage of the converter to match with the virtual generator armature voltage. In the next sections, the SM model used to implement the VSG in this paper will be addressed along with the additional controls and the power converter topology used for large-scale applications.

3.1 Machine model adopted in the VSG

To replicate the dynamic behavior of a SM, a high-order model is used to attain a greater response accuracy. The model implemented in Figure 4 is represented by Equations 1 and 2 with the addition of a set of equations representing the flux behavior in the SM windings. The chosen model uses four additional differential equations for this purpose besides the two equations of motion. Therefore, this model is often named a 6th order model (MACHOWSKI; BIALEK; BUMBY, 2008). The four equations that complete the model are given in Equations 17-20. Equations 21 and 22 are used to calculate the output armature voltages of the SM while Equation 23 calculates the output electrical power to serve as input in the swing Equation 1.

$$T'_{do}\dot{E}'_q = E_{fd} - E'_q + I_d(X_d - X'_d) \quad (17)$$

$$T'_{qo}\dot{E}'_d = -E'_d - I_q(X_q - X'_q) \quad (18)$$

$$T''_{do}\dot{E}''_q = E'_q - E''_q + I_d(X'_d - X''_d) \quad (19)$$

$$T''_{qo}\dot{E}''_d = E'_d - E''_d + I_q(X'_q - X''_q) \quad (20)$$

$$V_{td} = E''_d - X''_q I_q - I_d R_s \quad (21)$$

$$V_{tq} = E'_q + X''_d I_d - I_q R_s \quad (22)$$

$$P_e = E''_q I_q + E''_d I_d + (X''_d - X''_q) I_d I_q \quad (23)$$

where X_d and X_q are the synchronous reactances, X'_d and X'_q are the transient reactances, X''_d and X''_q are the subtransient reactances, T'_{do} and T'_{qo} are the open-circuit transient time constants, T''_{do} and T''_{qo} are the open-circuit subtransient time constants, the voltages represented by the letter E are the transient and subtransient machine voltages, P_e is the air-gap power of the SM, R_s is the armature resistance, I_d and I_q are the armature currents, V_d and V_q are the armature voltages. The suffixes d and q indicate the direct and quadrature axis respectively.

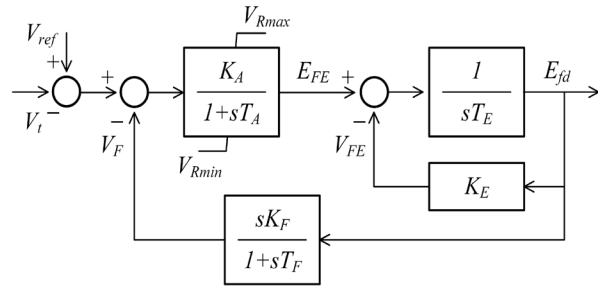
3.2 Additional voltage and frequency controls

The additional control loops shown in previous sections for the VSG are responsible for maintaining the machine synchronism with the grid and also controlling its output active and reactive power. This is accomplished by controlling the inputs of mechanical power and excitation field voltage in the virtual machine model. In this paper, the Governor used is based on a proportional droop control defined by Equation 24.

$$P_m = P_{Ref} + D_p f_n (1 - \omega) \quad (24)$$

where P_m is the generator's mechanical power input, P_{Ref} is the desired output power for the machine, f_n is the system nominal frequency in Hz, D_p is the droop gain, and ω is the rotor speed from the machine model. The AVR used is shown in Figure 5.

Figure 5 – AVR model used.



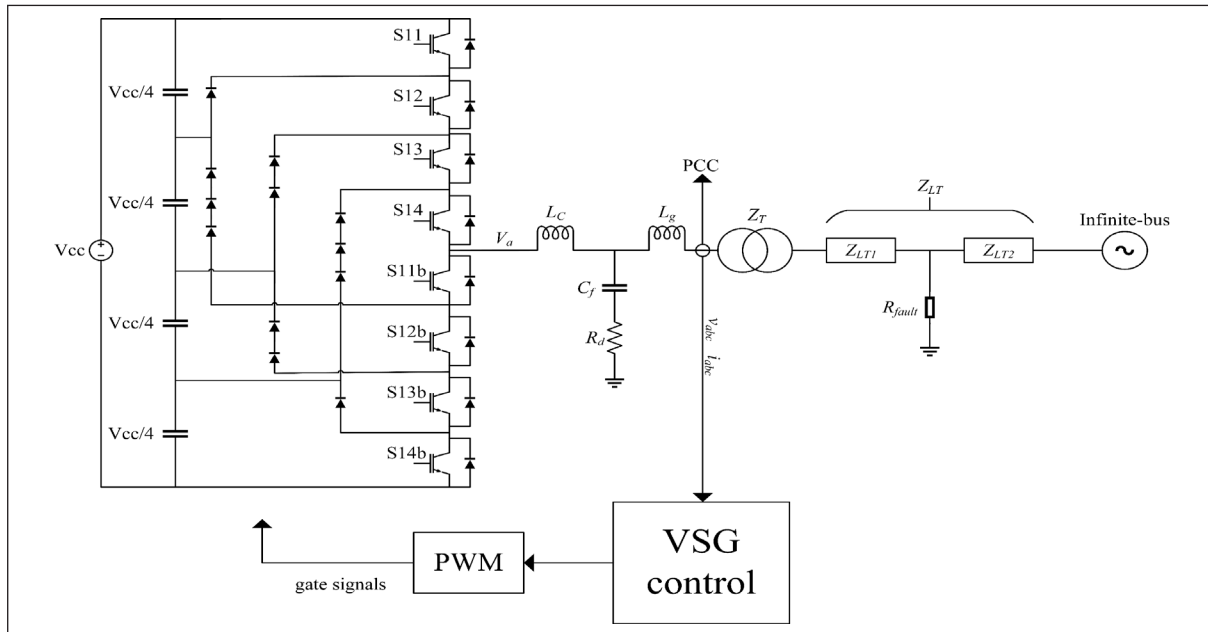
Source: adapted from Institute of Electrical and Electronics Engineers (2016).

The AVR is based on the DC1A excitation system defined by 421.5-2016 standard (INSTITUTE OF ELECTRICAL AND ELECTRONICS ENGINEERS, 2016). In order to simplify the model used, the limits of over and under excitation are neglected along with the exciter saturation effects. As a result, the system is comprised of a voltage regulator loop, a stabilization feedback loop, and the simplified model.

3.3 Power converter topology

In medium and high-voltage applications, the classic two-level voltage source inverter (VSI) is not an optimal and viable choice. For high voltage and power levels, the multilevel VSI converters are more suitable due to its reduced voltage stress in the semiconductor switches and higher efficiency with lower harmonic distortion on the PCC by using an adequate modulation technique (RODRIGUEZ et al., 2010). Thus, a 5-level neutral-point-clamped (NPC) converter is chosen to implement the power part of the VSG. Also, a phase disposition (PD) modulation technique is used. A single-phase representation of the SMIB system with the converter topology adopted is shown in Figure 6. A LCL-filter (LISERRE; BLAABJERG; HANSEN, 2005) was designed to filter the harmonics produced in the 5-level NPC converter switching.

Figure 6 – SMIB system with the 5-level NPC converter connected.



Source: authors.

4 Case study and simulation results

A SMIB system like the one in Figure 2 was simulated adopting the parameters presented in Table 1. This SMIB system was simulated for two different configurations. In the first configuration a traditional SM was connected at the machine bus, while in the second configuration, the VSG defined in Section 3 was connected. For each situation, six simulation scenarios were performed. The scenarios are defined by the distance of the fault from the generators and the level of power dispatched from the machines. The first three simulation scenarios are done with the fault

at the generator bus using a 0.2 p.u. impedance to the infinite bus and by changing the generator load P_{Ref} . In scenarios 4-6 the load change is also performed between scenarios but with an impedance between the generator bus and the fault. The CCTs obtained from each scenario in both situations are then compared and the results discussed. The LCL-filter parameters are also shown in Table 1.

In order to prove the equivalence between VSG and SM, the machine parameters used are the same in both configurations and are depicted in Table 2. The AVR and Governor parameters detailed in Table 3 are also the same in both systems.

Table 1 – LCL-filter and SMIB system simulation parameters.

Parameter	Value
SM and VSG power base (S_g)	100 MVA
SM and VSG voltage base (V_g)	18 kV
Transformer voltage ratio	18/230
Transformer power (S_T)	100 MVA
Transformer impedance (Z_T)	0.009 + j0.1 p.u.
Line impedance (Z_{LT})	0.0 + j0.4 p.u.
Fault resistance (R_{Fault})	1e-5 p.u.
LCL grid side impedance (Z_{Lg})	0.0 + j0.017 p.u.
LCL converter side impedance (Z_{Lc})	0.0 + j0.111 p.u.
LCL capacitance impedance (Z_c)	0.0 - j20.0 p.u.
LCL damping resistance (R_d)	0.179 p.u.

Source: authors.

Table 2 – Machine parameters used in VSG and SM.

Parameter	Value
Armature resistance (R_s)	0.002 p.u.
d-axis reactance (X_d)	0.92 p.u.
d-axis trans. reactance (X'_d)	0.3 p.u.
d-axis subtrans. reactance (X''_d)	0.22 p.u.
q-axis reactance (X_q)	0.504 p.u.
q-axis trans. reactance (X'_q)	0.201 p.u.
q-axis subtrans. reactance (X''_q)	0.132 p.u.
d-axis trans. open-circuit time cte. (T'_{do})	5.2 s
q-axis subtrans. open-circuit time cte. (T''_{qo})	0.85 s
d-axis subtrans. open-circuit time cte. (T'''_{do})	0.029 s
q-axis subtrans. open-circuit time cte. (T'''_{qo})	0.034 s

Source: authors.

Table 3 – AVR and Governor parameters.

Parameter	Value
Frequency droop gain (D_p)	2.0
Nominal grid frequency (f_p)	60.0 Hz
Voltage reference (V_{Ref})	1.0 p.u.
Voltage regulator gain (K_A)	100.0 p.u.
Voltage regulator time constant (T_A)	0.001 s
Feedback loop gain (K_p)	0.001 p.u.
Feedback loop time constant (T_p)	0.1 s
Exciter gain (K_E)	1.0 p.u.
Exciter time constant (T_E)	0.1 s

Source: authors.

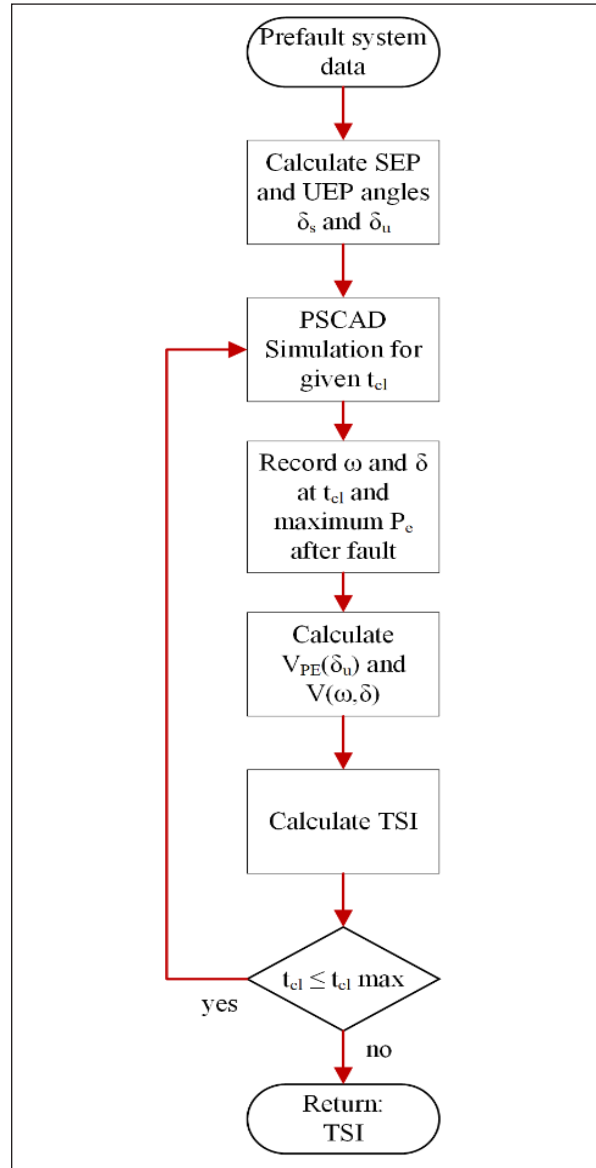
4.1 Simulation steps

The simulations were carried out in two different softwares. The PSCAD was used to simulate both SM and VSG and compare their transient responses. To validate the analytical CCT calculated, the Power System Analysis Toolbox (PSAT) for MATLAB was used. During the first seconds of PSCAD simulation, the VSG is synchronized to the grid and maintained in steady-state by the AVR and Governor controls. In all scenarios, a three-phase fault is applied at 7.5 s. At this moment, the AVR and Governor control actions are suppressed and the field excitation voltage E_{fd} and mechanical power input P_m are made constant and equal to their steady-state values before the fault occurrence.

As a result, only the machine modelling and its inertia are considered for the system CCT definition. The theoretical CCT is calculated from Equations 15 and 16 using the value of δ_0 calculated using the information in Tables 1, 2, and 4. In the scenarios where the TSI is calculated, the process begins by calculating the system SEP defined by δ_s and UEP defined by δ_u using Equations 7, 8, and 12. After this step, the energy at the UEP is calculated using Equation 6 by the sum of the potential terms. The Pe_{fault}^{max} value is obtained as the maximum first-swing output power recorded from the system post-fault response in the simulation.

The VSG and SM rotor angle and speed are recorded in the simulation fault clearance time instant. The transient energy is calculated using complete Equation 6. The TSI is calculated by Equation 11 using the energy in the UEP and the energy obtained in the fault extinction moment. The flowchart shown in Figure 7 is used to demonstrate the TSI calculation sequence.

Figure 7 – TSI calculation flowchart.



Source: authors.

4.2 Simulation results and discussion

The CCT obtained from the different simulations and the calculated theoretical values are presented in Table 4. From the CCT values in Table 4, it can be seen that the VSG system remains stable for very similar fault duration times to that of the traditional SM system. The $\Delta(\%)$ column in Table 4 shows the percentage differences found between the CCT obtained from the VSG and SM PSCAD simulations, calculated using Equation (25). It can be seen that the maximum difference from all scenarios is around 5.785%, which shows the good proximity in the transient stability of both systems.

The swing curves and kinetic energy from scenarios 2 and 4 are shown in Figures 8 and 9, respectively, for different values of t_{cr} . The graphs in Figure 8 (a) and (b) show similar behavior for both systems in scenario 2 with a more damped post-fault oscillatory response for the VSG, especially the result observed in the kinetic energy.

The VSG post-fault kinetic energy also shows an oscillation frequency slightly higher than the SM response. This result is also observed in the curves for scenario 4 in Figure 9 (a) and (b). In this case, the damping is less noticeable in the kinetic energy oscillations and the frequency does not show the same divergence levels. Additionally, both scenarios show a small difference in the rotor angle at the start of the faulted period for the VSG and SM systems.

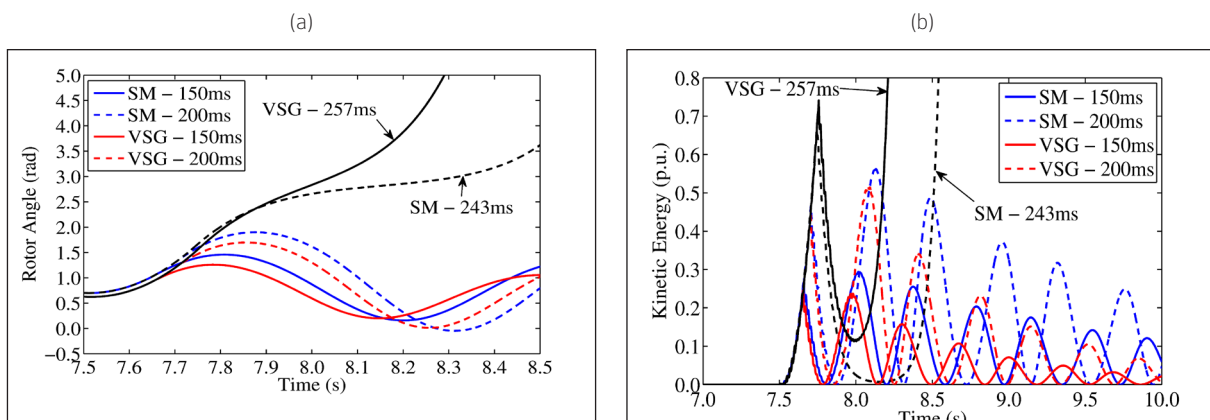
$$\Delta(\%) = \frac{CCT(VSG) - CCT(SM)}{CCT(SM)} \times 100\% \quad (25)$$

Table 4 – Simulated scenarios and CCT values obtained.

Scn.	P_{Ref} (p.u.)	Z_{LT1} (p.u.)	Z_{LT2} (p.u.)	CCT (s)				Δ (%) (VSG/SM)
				Calculated	PSAT	SM	VSG	
1	1.0	0.0	j0.2	0.176	0.178	0.181	0.189	4.419
2	0.8	0.0	j0.2	0.229	0.217	0.242	0.256	5.785
3	0.5	0.0	j0.2	0.354	0.345	0.392	0.392	0.000
4	1.0	j0.2	j0.2	0.123	0.121	0.123	0.125	1.626
5	0.8	j0.2	j0.2	0.182	0.168	0.183	0.188	2.732
6	0.5	j0.2	j0.2	0.317	0.321	0.329	0.327	-0.607

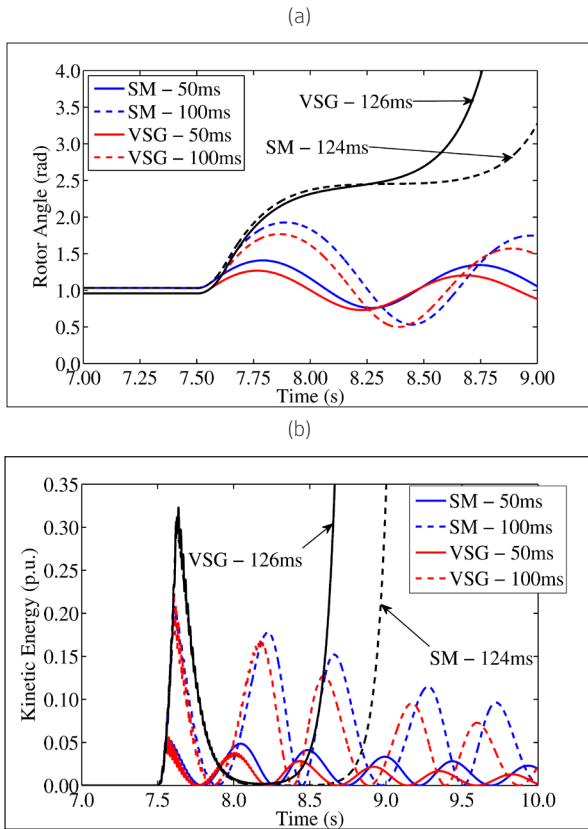
Source: authors.

Figure 8 – System swing curves (a) and kinetic energy (b) for scenario 2.



Source: authors.

Figure 9 – System swing curves (a) and kinetic energy (b) for scenario 4.



Source: authors.

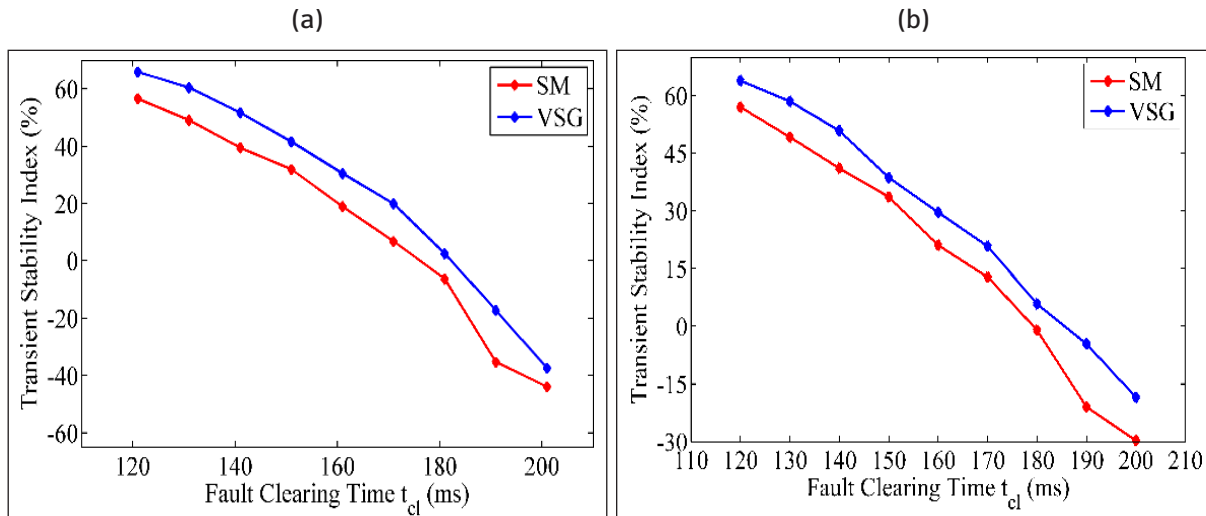
At the moment of fault clearance, the two systems reach similar values of rotor angle and kinetic energy, and as a result, this makes the system display the similarity in CCT observed in Table 4 and the similar behavior in TSI that is illustrated in Figure 10.

Figure 10 (a) and (b) show a TSI comparison between VSG and SM for scenarios 1 and 5 for a variation of t_{cl} using steps of 10 ms. By choosing different scenarios, the comparison between SM and VSG can be done for different generator loading and line impedance configurations. Observing the graphs, a resemblance between the TSI curve from the VSG system and the SM system can be seen with a small visible vertical offset between them.

This result reveals that the VSG-based control is equivalent to the SM not just at CCT, but it displays a transient energy margin that is close to the SM for different values of fault duration. Therefore, the VSG distances itself from the UEP with similar energy levels to that of a SM.

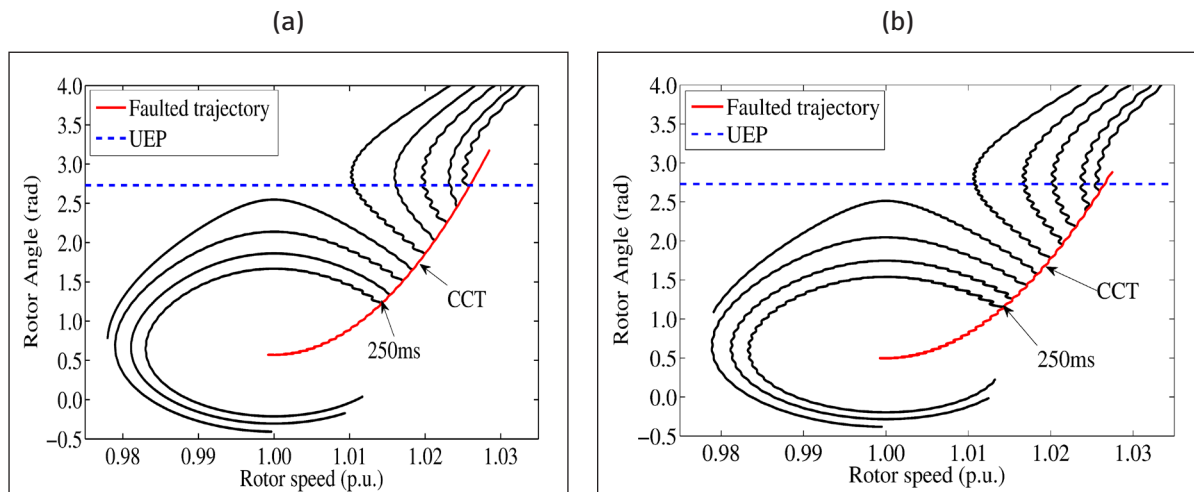
Figure 11 (a) and (b) portray the trajectory of both systems in the phase plane (ω, δ). The graphs were plotted from simulations in scenario 6 by varying the from 250 ms to 450 ms with steps of 25 ms. Despite the little divergences observed in some of the results in Figures 8-10, it can be seen in Figure 11 graphs (a) and (b) that both VSG and SM developed correspondent trajectories in the phase plane for the various clearing times simulated, which in turn corroborates the results obtained via CCT analysis.

Figure 10 – Comparative TSI curves. (a) Scenario 1. (b) Scenario 5.



Source: authors.

Figure 11 – Phase plane faulted and post-fault trajectory curves. (a) SM. (b) VSG.



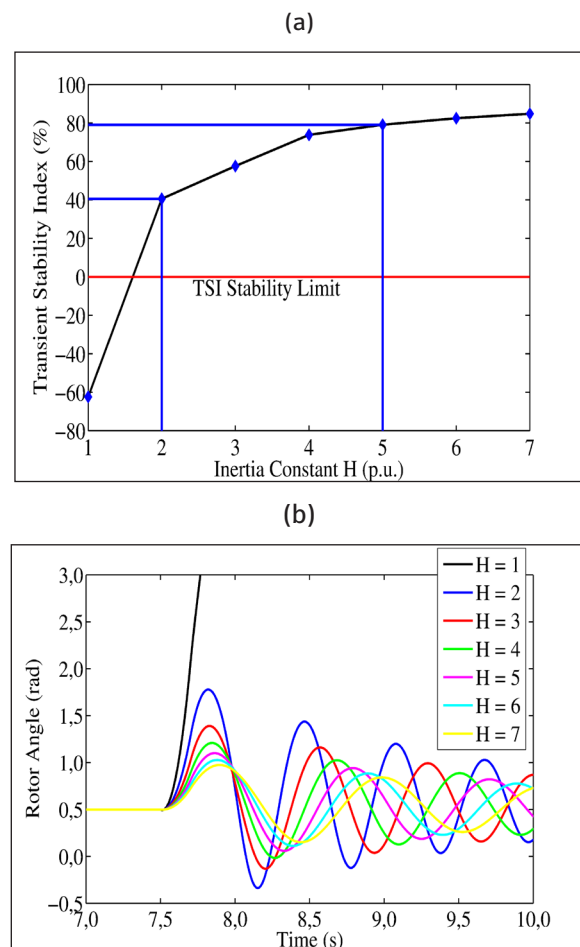
Source: authors.

This outcome evidenced by Figures 8-11 and by Table 4 proves the electrodynamic equivalence of the VSG-based power converter with a traditional SM, which in turn shows that a VSG is capable of supporting the system transient stabilization.

To evaluate the potential of an adaptive control for the VSG, a simulation scenario was developed in which is kept constant and the VSG system is simulated for different inertia constant values. In Figure 12, graph (a) shows a curve for TSI on scenario 6 for H varying from 1 to 7 p.u., while graph (b) shows the swing curves for the same circumstances. In both graphs, the fault clearing time is kept constant at 200 ms. All VSG parameters were the same as indicated in Table 2 except for the inertia constant.

The results presented in both graphs show that varying one of the VSG parameters can alter the system stability margin. It can be seen that the TSI increases with the increment in H while the swing curves experience lower excursions in the rotor angle peak value in time. This parameter change, especially the inertia constant, must respect the converter DC-link energy capabilities.

Figure 12 – Adaptive inertia control curves: (a) TSI curve. (b) Swing curves.



Source: authors.

The sizing of the energy storage device used for this type of application must consider the adaptive parameter control. The results indicate a real possibility to change the VSG contribution for transient stability during its operation by adopting adequate adaptive control for the inertia constant. It can be seen from Figure 12 graph (a) that for an initial system configuration ($H = 1$), the system is in the unstable region ($TSI = -60\%$). Thus, a proper adaptive control could alter the VSG parameters by changing the virtual inertia constant ($H = 2$), for example, in order to lead the system to a stable region ($TSI = 40\%$).

Furthermore, this proposal studied opens the possibility for a quantitative approach to implement a real-time system stability margin adaptive control. For example, it can be seen from Figure 12 graph (a) that the stability margin could be tuned between 40% and 80% by adjusting the virtual inertia constant ($H = 2$ to 5). However, a saturation in the TSI curve is observed for higher values of virtual inertia ($H > 5$). Hence, an adaptive control should be designed to maintain the system in optimal values of energy margin, between the stability limits and the saturation boundary.

5 Conclusions

This paper evaluated the contribution for transient stability of a LS-RES power converters control based on the virtual synchronous machine outline. A methodology for implementing this control was presented and validated through simulation results using transient stability metrics, the TSI, and the CCT.

The TEF method for transient stability assessment was described and the results for the TSI values encountered show great proximity between the VSG and the traditional SM energy margin. The dynamic response of the VSG-based control offered a high similarity with the response of a traditional SM, which can also be observed by the CCT values found in the simulations. Despite some divergences in the post-fault oscillatory responses, the trajectory curves proved the equivalence of the systems when analyzed via phase-plane. The combined results reveal the ability of the VSG to support the power system stabilization in the occurrence of large-disturbances.

The parameters adaptability of the VSG-based control was analyzed and proved to be a promising alternative to enhance the transient response of this type of power converters control for large-scale non-rotational generating units.

To further develop the issue discussed in this paper, adaptive controls could be proposed to improve the transient stability of VSG converters by changing parameters such as the inertia constant H and the electrical model parameters.

ACKNOWLEDGEMENT

This study was financed in part by the Coordenação de Aperfeiçoamento de Pessoal de Nível Superior - Brasil (CAPES) - Finance Code 001, Fundação de Amparo à Pesquisa e Inovação do Espírito Santo - Finance Codes 117/2019 and 536/2018.

REFERENCES

- ALIPOOR, J.; MIURA, Y.; ISE, T. Power system stabilization using virtual synchronous generator with alternating moment of inertia. **IEEE Journal of Emerging and Selected Topics in Power Electronics**, v. 3, n. 2, p. 451-458, jun. 2015.
- ANTÓNIO-FERREIRA, A.; COLLADOS-RODRÍGUEZ, C.; GOMIS-BELLMUNT, O. Modulation techniques applied to medium voltage modular multilevel converters for renewable energy integration: a review. **Electric Power Systems Research**, v. 155, p. 21-39, 2018.
- BECK, H.-P.; HESSE, R. Virtual synchronous machine. In: 2007 9th INTERNATIONAL CONFERENCE ON ELECTRICAL POWER QUALITY AND UTILISATION, 2007, Barcelona (Spain), **Proceedings...** 2007.
- BUENO, P. G.; HERNÁNDEZ, J. C.; RUIZ-RODRIGUEZ, F. J. Stability assessment for transmission systems with large utility-scale photovoltaic units. **IET Renewable Power Generation**, v. 10, n. 5, p. 584-597, 2016.
- CABRERA-TOBAR, A. et al. Review of advanced grid requirements for the integration of large scale photovoltaic power plants in the transmission system. **Renewable and Sustainable Energy Reviews**, v. 62, p. 971-987, 2016.
- CARRARA, G. et al. A new multilevel PWM method: a theoretical analysis. **IEEE Transactions on Power Electronics**, v. 7, n. 3, p. 497-505, 1992.
- CHOWDHURY, M. A. et al. Comparative study on fault responses of synchronous generators and wind turbine generators using transient stability index based on transient energy function. **International Journal of Electrical Power & Energy Systems**, v. 51, p. 145-152, 2013.

- DING, M. et al. A review on China's large-scale PV integration: progress, challenges and recommendations. **Renewable and Sustainable Energy Reviews**, v. 53, p. 639-652, 2016.
- DRIESEN, J.; VISSCHER, K. Virtual synchronous generators. In: 2008 IEEE POWER AND ENERGY SOCIETY GENERAL MEETING - CONVERSION AND DELIVERY OF ELECTRICAL ENERGY IN THE 21ST CENTURY, 2008, Pittsburgh (United States), **Proceedings...** 2008.
- EFTEKHARNEJAD, S. et al. Impact of increased penetration of photovoltaic generation on power systems. **IEEE Transactions on Power Systems**, v. 28, n. 2, p. 893-901, 2013.
- ENCARNAÇÃO, L. et al. Virtual inertia for power converters control. In: YAHYAOU, I. (Ed.). **Advances in renewable energies and power technologies**. Volume 2: biomass, fuel cells, geothermal energies, and smart grids. 1. ed. [s.i.]: Elsevier Science, 2018. p. 377-411. Ch. 11.
- FOUAD, A. A.; VITTAL, V. The transient energy function method. **International Journal of Electrical Power & Energy Systems**, v. 10, n. 4, p. 233-246, 1988.
- GAUTAM, D.; VITTAL, V.; HARBOUR, T. Impact of increased penetration of DFIG-based wind turbine generators on transient and small signal stability of power systems. **IEEE Transactions on Power Systems**, v. 24, n. 3, p. 1426-1434, ago. 2009.
- GRAINGER, J. J.; STEVENSON, W. D. **Power system analysis**. 1. ed. Singapore: McGraw-Hill, 1994.
- INSTITUTE OF ELECTRICAL AND ELECTRONICS ENGINEERS. **IEEE. 421.5-2016** - IEEE recommended practice for excitation system models for power system stability studies. Revision of IEEE Std 421.5-2005. IEEE, 2016.
- KUNDUR, P. et al. Definition and classification of power system stability. **IEEE Transactions on Power Systems**, 2004.
- KUNDUR, P. **Power system stability and control**. 1. ed. New York (United States): McGraw-Hill, 1994.
- PVRESOURCES. **Large-scale PV power plants - Top 50**. Disponível em: <<http://www.pvresources.com/en/top50pv.php>>. Acesso em: jun. 2020.
- LI, D. et al. A self-adaptive inertia and damping combination control of VSG to support frequency stability. **IEEE Transactions on Energy Conversion**, v. 32, n. 1, p. 397-398, mar. 2017.
- LISERRE, M.; BLAABJERG, F.; HANSEN, S. Design and control of an LCL-filter-based three-phase active rectifier. **IEEE Transactions on Industry Applications**, v. 41, n. 5, p. 1281-1291, 2005.
- MACHOWSKI, J.; BIALEK, J. W.; BUMBY, J. R. **Power system dynamics: stability and control**. 2. ed. West Sussex (United Kingdom): Wiley, 2008.
- MCGRATH, B. P.; HOLMES, D. G. Multicarrier PWM strategies for multilevel inverters. **IEEE Transactions on Industrial Electronics**, v. 49, n. 4, p. 858-867, 2002.
- RODRIGUEZ, J. et al. A survey on neutral-point-clamped inverters. **IEEE Transactions on Industrial Electronics**, v. 57, n. 7, p. 2219-2230, 2010.
- SAUER, P. W.; PAI, M. A.; CHOW, J. H. **Power system dynamics and stability: with synchrophasor measurement and power system toolbox**. Hoboken (United States): Wiley, 2017.
- SHAH, R. et al. A review of key power system stability challenges for large-scale PV integration. **Renewable and Sustainable Energy Reviews**, v. 41, p. 1423-1436, 2015.
- SHI, L. et al. Effects of wind generation intermittency and volatility on power system transient stability. **IET Renewable Power Generation**, v. 8, n. 5, p. 509-521, 2014.
- TAN, Y. T.; KIRSCHEN, D. S. Impact on the power system of a large penetration of photovoltaic generation. 2007 IEEE POWER ENGINEERING SOCIETY GENERAL MEETING, 2007, Tampa (United States), **Proceedings...** 2007.
- TORRES L., M. A. et al. Self-tuning virtual synchronous machine: a control strategy for energy storage systems to support dynamic frequency control. **IEEE Transactions on Energy Conversion**, v. 29, n. 4, p. 833-840, 2014.
- XUE, Y.; VAN CUSTEM, T.; RIBBENS-PAVELLA, M. Extended equal area criterion justifications, generalizations, applications. **IEEE Transactions on Power Systems**, v. 4, n. 1, p. 44-52, 1989.